Oblique slip on long faults enables a continuum of earthquake rupture speeds

Huihui Weng[1*] and Jean-Paul Ampuero[1]

[1] *Université Côte d'Azur, IRD, CNRS, Observatoire de la Côte d'Azur, Géoazur, 250 rue Albert Einstein, Sophia Antipolis, 06560 Valbonne, France*

Correspondence to Huihui Weng (email: weng@geoazur.unice.fr)

Seismological observations show that large earthquakes span a continuum of rupture speeds, ranging from slower than Rayleigh wave speeds to P wave speed, and including speeds that are predicted to be unstable by 2D theory. Earthquake rupture speed controls ground shaking and thus seismic hazard, yet a quantitative model reconciling the observations and basic theory is still missing. Here we show that long ruptures with oblique slip can propagate steadily at a variety of speeds, even in the range of previously-suggested unstable speeds. The obliqueness of slip and the ratio of fracture energy to static energy release rate primarily control the propagation speed of long ruptures. We find that their effects on rupture speed can be well predicted by extending the 3D theory of fracture mechanics to long, mixed-mode shear ruptures. The basic model developed here provides a new quantitative framework to interpret supershear earthquakes, to constrain the energy ratio of faults based on observed earthquake rupture speed and rake angle, and to forecast future rupture speeds and sizes based on the observed slip deficit along faults.

Introduction

Earthquake rupture speed affects ground shaking and thus seismic hazard, yet the quantitative factors controlling the rupture speed of large earthquakes are still not completely understood and the speeds of some earthquakes remain to be reconciled with basic models. In general, faster ruptures generate stronger ground shaking, near to and far from the fault[1–3]. A compilation of earthquake rupture speeds estimated from seismological observations[4–11] (Fig 3a) illustrates that most earthquakes propagate at speeds slower than the shear wave speed, v_S, and some[8,9] at speeds faster than the Eshelby speed, $v_E = \sqrt{2}v_S$ (hereafter called “fast supershear” earthquakes). Recent evidence[4,5] shows that supershear earthquakes can also propagate steadily at sub-Eshelby speed (hereafter called “slow supershear”), which is unexpected from the 2D theory of fracture mechanics[12]. Such unexpected speeds have been reported in large earthquakes, whose ruptures are much longer than wide[13,14]. The propagation of ruptures with large aspect ratio has been studied theoretically in 3D in mode III, corresponding to pure-dip-slip faulting[15]. By extending that theory to 3D mode II ruptures, we found that slow supershear speeds are also inadmissible for long, steady, pure-strike-slip earthquakes (Methods A3), as in the 2D theory. However, natural earthquakes generally have oblique slip, with both strike-slip and dip-slip components[13]. A 2D theoretical study[16] suggested that such mixed-mode ruptures can propagate at speeds between the Rayleigh wave speed v_R and v_S, which is a “forbidden zone” for pure mode II rupture. Such speeds have been observed in 3D numerical simulations only during very short transients that would be difficult to observe in nature[17]. Here, we show that large mixed-mode earthquakes can propagate steadily at speeds spanning the continuum of speeds observed in nature, including “forbidden” and slow supershear speeds.

Rake angle and energy ratio control rupture speed

The propagation of long mixed-mode ruptures (Fig 1) is controlled primarily by two dimensionless quantities, as deduced by dimensional analysis and confirmed by numerical simulations (Methods A1): the rake angle θ between the initial fault traction and the horizontal direction, and the energy ratio G_c/G_0 between dissipated and potential energies. Here, G_c is the fracture energy dissipated near the rupture front and G_0 is the static energy release rate of mode III subshear ruptures. The latter depends on stress drop and rupture width W, but not on rupture length[15]. A third non-dimensional parameter, the ratio L_c/W between the size of the weakening process zone at the rupture tip and the rupture width, has a secondary effect on the asymptotic rupture behavior[18]. Five different rupture behaviors emerge in 3D numerical simulations as the two primary control parameters are systematically varied (Fig 2a). We first identify two large classes: self-arresting ruptures decelerate and eventually stop spontaneously, while runaway ruptures propagate unabated through the entire fault and eventually approach a steady rupture speed (Fig 2b). We further classify runaway ruptures according to their steady speed: subshear, "forbidden", slow-supershear and fast-supershear ruptures.

Remarkably, long ruptures can propagate steadily at a variety of speeds faster than the Rayleigh wave speed, even at slow supershear speeds and in the "forbidden" zone (Fig 2b). The steady speed of subshear ruptures is v_R for mode II (strike-slip), v_S for mode III (dip-slip), and lies between the two for mixed mode (oblique slip)[16]. The steady speeds of supershear ruptures lie between v_S and v_P and decrease as the rake angle and energy ratio increase (Fig 2c). The same rupture behaviours are identified on the basis of the apparent horizontal speed (Methods A2), a quantity more usually constrained by seismological analyses, except that apparent horizontal speeds in the "forbidden" zone are not found (Fig S2).

The conditions separating the different rupture behaviors can be understood and quantitatively predicted by extending the theory of fracture mechanics to 3D mixed-mode long ruptures. A basic element of the theory is that the energy release rate for mixed-mode rupture is the sum of the mode II and mode III contributions. For steady subshear ruptures, it is of the form $G^{mix} = G_0 f(\theta)$ (Methods A4). Ruptures are runaway if their energy release rate exceeds the fracture energy, $G^{mix} > G_c$, otherwise they are self-arresting. Thus the boundary between self-arresting and runaway ruptures satisfies $G_c = G^{mix}$:

$$G_c/G_0 = f(\theta) = (1-\nu)^{-1}\cos^2\theta + \sin^2\theta \tag{1}$$

where $\nu = 0.25$ is Poisson's ratio, which is in good agreement with our 3D dynamic simulations results (Fig 2a). For steady supershear ruptures, the energy release rate is of the form $G^{mix} = G_0 f(\theta, v_r)$. The values of $f(\theta, v_r)$ at $v_r = v_E$ and $v_r = v_S$ are determined theoretically (Methods A4) and, in combination with the steady energy balance $G_c = G^{mix}$, the boundaries between slow and fast supershear ruptures and between slow supershear and "forbidden" ruptures are well predicted (Fig 2a).

Ruptures with oblique slip can propagate steadily at slow supershear and "forbidden" speeds because their rupture fronts are not vertical but tilted (Fig 2d & S1b). A kinematic model that captures purely geometrical effects, considering an expanding elliptical front with obliquely oriented major axis (Fig S4), qualitatively explains the occurrence of unexpected speeds on long faults but also shows substantial discrepancies with the dynamic model (Methods A6). Fracture dynamics theory provides a mechanical explanation for the existence of steady rupture speeds in the "forbidden" zone. While the mode III contribution to the energy release rate is negative in the "forbidden" zone, in a tilted mixed-mode rupture front it is compensated by the positive mode II contribution (Methods A4), thus enabling a steady energy balance $G^{mix} = G_c$.

Seismological observations of supershear ruptures

The theory developed here provides a new interpretive framework for supershear earthquakes that suggests a method to constrain the energy ratio G_c/G_0 of faults based on observations of earthquake rupture speed and rake angle. Model and observations can be compared in terms of rupture speed, rake angle and energy ratio (Fig 3a). All the supershear earthquakes observed so far have rake angles lower than 60° and a continuum of rupture speeds up to v_P. The basic model well explains these earthquake observations and constrains the energy ratios of faults to lie between 0.5 and 0.89. For energy ratios smaller than 0.5, supershear speeds are, in theory, allowed over a wider range of rake angles (dashed curves in Fig 3a; Methods A1) but have not been observed in nature (Fig 3a). A recent example of slow supershear rupture is the 2018 Mw7.5 Palu earthquake, which was inferred to propagate steadily at a sub-Eshelby speed ∼4.1 km/s[5,19]. Considering the rakes constrained by different studies of the Palu earthquake (∼25°[19], ∼6-15°[14], and ∼15-17° from

USGS and gCMT), such slow supershear rupture requires an energy ratio between 0.75 and 0.85. An alternative interpretation of the unusual speed of this earthquake assumes the presence of a low velocity fault zone[20], which remains to be confirmed by local fault studies. The 2013 Mw6.7 Okhotsk deep earthquake[6] and the 1999 Mw7.5 Turkey Izmit earthquake[7] were estimated to propagate at Eshelby speed. This requires values of rake angle and energy ratio near the boundary between slow and fast supershear ruptures. The rake angle of these two events are very close to mode II ruptures[6,13]. Thus, if these ruptures have a steady Eshelby speed, their energy ratio should be around 0.89 (Fig 2a); if their speed is not steady and the rupture comprises both super-Eshelby and subshear segments, this value is an upper bound on the energy ratio for the fault segments with super-Ehshelby speed. An example of fast supershear rupture is the 2001 Mw8.1 Kunlun earthquake[8]. An intermediate portion of the rupture had super-Eshelby speed ∼5 km/s and rake ∼10°[13], which requires $0.7 < G_c/G_0 < 0.8$.

The model presented here also explains the continuum of earthquake rupture speeds, ranging from slower than Rayleigh wave speeds to P wave speed (Fig 3b). For subshear runaway ruptures, steady propagation at speeds arbitrarily lower than the shear wave speed requires the fracture energy to increase with rupture speed, which can result from velocity-dependent friction[15]. Otherwise, subshear runaway ruptures accelerate to a rake-dependent steady speed between v_R and v_S and, for a given rupture length, their average rupture speed increases from 0 to v_S as the energy ratio decreases. In the "forbidden", slow-supershear and fast-supershear regimes, ruptures can propagate steadily at speeds between v_R and v_P, even in the absence of velocity-dependent friction: they are stable because the velocity-dependence of energy release rate can stabilize perturbations of rupture speed (Methods A3).

Implications for physics-based seismic hazard assessment

The fracture mechanics theory of long ruptures developed here provides a physics-based framework to relate the time-dependent seismic hazard along large faults to quantities that can be observed and monitored, such as seismic coupling (Fig 4). A rupture potential Φ was introduced by Weng and Ampuero[15] to infer the arrest distance of long dip-slip (mode III) ruptures with a given spatial distribution of G_c/G_0 along strike. We adapt their definition to mixed-mode long faults as:

$$\Phi(L_1, L_2) = \int_{L_1}^{L_2} (1 - G_c/G^{mix}) dL/W \tag{2}$$

where $G^{mix} = G_0 f(\theta)$ is the energy release rate for mixed-mode steady subshear ruptures and W is the rupture width. The rupture potential serves to anticipate the final size of a rupture: a rupture can propagate over the entire fault segment $[L_1, L_2]$ only if $\Phi(L_1, L_2) > 0$, i.e., if the average of the mixed-mode energy ratio G_c/G^{mix} along the segment is < 1. In addition, if G_c/G^{mix} is much smaller than 1, such as in the slow-supershear and fast-supershear regimes in Fig. 3b, the rupture of the entire fault segment can be supershear. Therefore, two properties that strongly affect the seismic hazard of a given fault, namely rupture length and speed, can be assessed from estimates of the rake angle θ and the energy ratio G_c/G_0 along the fault. The rake angle can be estimated from geodetic data. We propose below an approach to estimate the energy ratio at each along-strike location on long faults.

On the one hand, G_0 on long faults is approximately related to final slip D by $G_0 =$

$C\mu D^2/W$, where C is a geometrical factor of order 1 (Methods A5). On the other hand, fracture energy G_c can be estimated from scaling relations as a function of final slip D. Such relations have been derived over a wide range of earthquake sizes by different approaches: dynamic earthquake modeling[21–23], laboratory experiments[24], and seismological methods such as kinematic source inversion[25,26] (Fig 4a). As a crude first-order approximation, we seek a scaling relation of the form $G_c \approx BD^n$. Theoretical models with off-fault inelastic dissipation[1,27] lead to $n = 1$ and for thermal pressurization[25] $n = 2/3$. As we focus here on large earthquakes, we only consider the data with $D > 0.1$ m. We ignore the data of kinematic source inversions which are likely to overestimate the fracture energy due to their over-smoothing of the slip rate function[22]. Least squares regression gives $n = 0.7$ and $B = 3$ (the units of G_c and D are MJm^{-2} and m, respectively).

The resulting relation between energy ratio and slip is: $G_c/G_0 = BWD^{n-2}/C\mu$. The spatial distribution of slip deficit rate along a fault can be inferred from geodetic observations[28–30]. Given an estimate of slip deficit at a future time, a worst-case scenario (largest possible magnitude) is obtained by assuming all the slip deficit is released by a single large earthquake, i.e., D is set equal to the slip deficit. Because G_0 depends more strongly than G_c on D ($n < 2$), the energy ratio G_c/G_0 decreases with increasing slip deficit D. Thus the condition for runaway ruptures (equation (1)) predicts that fault segments need to accumulate a certain critical slip deficit $D^{run}(\theta)$ to become capable of hosting long runaway ruptures, otherwise they can only host self-arresting ruptures. Combining the scaling relation of energy ratio versus slip with equation (2) allows to infer the largest possible rupture size from a slip deficit distribution. As an illustration, the time-dependent evolution of the segmentation of the central Andes subduction zone in Chile predicted by the model is shown in Fig 4c, and yields a reasonable estimate of return time of a 1960-like mega-earthquake of $\sim$360 yrs ($250 - 500$ yrs, accounting for model uncertainties). Similarly, a minimum slip deficit value $D^{sup}(\theta)$ is required for steady supershear ruptures (Methods A4). The model also implies that, on a given fault, supershear earthquakes should have larger slip than subshear ones.

Future efforts to establish robust scaling relations between fracture energy and slip, from synergistic developments of frictional theories, laboratory experiments and seismological observations, should allow to integrate the concepts presented here into earthquake hazard assessment. Concretely, based on the spatial distribution of slip deficit rate inferred from geodetic data, the proposed analysis would allow to partition a fault into segments with different potential behaviors in future earthquakes: self-arresting or runaway, subshear or supershear. By accounting for the finite width of seismogenic zones and the obliqueness of earthquake slip, our findings quantitatively reconcile the observations of earthquake rupture speeds with the basic theory of rupture dynamics while opening new avenues for physics-based seismic hazard assessment.

Methods

A1. Dynamic rupture simulations. We set 3D dynamic rupture simulations with oblique slip on a long fault with finite seismogenic width W embedded in an unbounded, linear elastic, homogeneous medium. We use a computational domain large enough to avoid the effects of the reflected waves from the domain boundaries within the simulation time. We assume a Poisson's ratio ν of 0.25. The shear modulus and S wave speed of the medium are denoted μ and v_S, respectively. The P wave speed, the Eshelby speed, and the Rayleigh wave speed are $v_P = \sqrt{3}v_S$, $v_E = \sqrt{2}v_S$, and $v_R = 0.92v_S$, respectively.

We use the linear slip-weakening friction law with slip-weakening distance d_c, static strength τ_s, and dynamic strength τ_d. This is the most simple friction law adopted in computational earthquake dynamics, and allows to prescribe a constant fracture energy $G_c = 0.5d_c(\tau_s - \tau_d)$. The strength values are also fixed because the fault normal stress is constant due to the symmetries of the problem. For a pure-dip-slip fault (rake angle of 90°), Weng and Ampuero[15] demonstrated that the key parameter that controls the evolution of rupture speed is the energy ratio G_c/G_0^{III}, where the energy release rate is $G_0^{III} = \lambda_{III}\Delta\tau^2 W/\mu$ and $\Delta\tau = \tau_0 - \tau_d$ is the nominal stress drop and λ_{III} a geometric factor of order 1. The definition of the mode II energy ratio G_c/G_0^{II} is the same[31] except for the value of the geometric factor λ_{II}. The energy ratio for purely mode II or purely mode III (assuming the same stress drop $\Delta\tau$) can be written as:

$$\frac{G_c}{G_0^*} = \frac{1}{2\lambda^*}\frac{L_c}{W}\left[\frac{\Delta_\tau}{\tau_s - \tau_d}\right]^{-2}, \tag{3}$$

where

$$L_c = \frac{\mu d_c}{\tau_s - \tau_d} \tag{4}$$

is a characteristic frictional length proportional to the static cohesive zone size[32], $\lambda^* = \lambda_{II}$ for mode II and $\lambda^* = \lambda_{III}$ for mode III. The value of λ_{III} was determined analytically and validated numerically[15]: $0.96/\pi$ for a deep buried fault (infinite space, like considered here), $1.92/\pi$ for a surface-breaking fault in a half-space, and between $0.96/\pi$ and $1.92/\pi$ for a buried fault in a half-space. Here, we found numerically for mode II ruptures on a deep buried fault that $\lambda_{II} \approx 0.96/\pi/(1-\nu)$, which is similar to the value 0.43 obtained by Weng and Yang[31]. Then we have $\lambda_{II}/\lambda_{III} = (1-\nu)^{-1}$. In the main text, we denote $G_0 = G_0^{III}$, and thus $G_0^{II} = (1-\nu)^{-1}G_0$. To prescribe the energy ratio G_c/G_0, we fix the value of the *cohesive ratio* $L_c/W = 0.25$ and vary the stress ratio $\Delta\tau/(\tau_s - \tau_d)$. Note that here we denote $\Delta\tau$ the absolute amplitude of stress drop. The minimum value of the energy ratio is proportional to the *cohesive ratio*, $G_c/G_0 \propto L_c/W$, and is obtained when the stress drop $\Delta\tau$ equals the strength drop $\tau_s - \tau_d$ (in such extreme case, the P wave from the hypocenter can trigger the rupture of the entire fault, enabling rupture at the P wave speed for all mixed-mode ruptures). Since we consider oblique slip with rake angle θ (the direction between the initial traction vector and the horizontal direction), the initial shear stress, whose amplitude is τ_0, has an along-strike component $\tau_0 \cos\theta$ and along-dip component $\tau_0 \sin\theta$. Exploiting the symmetries of the problem, we only need to simulate rake angles between 0° and 90°. Other values θ' between -180° and 180° can be mapped to the 0-90° range as $\theta = min(|\theta'|, 180 - |\theta'|)$. If the absolute initial stress τ_0 is too small compared to the stress drop $\Delta\tau$, the slip direction may be time-dependent inside the cohesive zone[16] and thus the actual fracture energy may be larger than G_c. To have full control on the actual value of the fracture energy, we set up a relatively large initial stress, $\tau_0/\Delta\tau \approx 10$.

We prescribe a time-dependent weakening over the nucleation zone of size $L/W = 2$ to nucleate unilateral ruptures at prescribed speeds. Rupture propagation becomes spontaneous outside the nucleation zone. To study steady supershear ruptures, without focusing on the supershear transition, we set the nucleation speed as $1.1v_S$ or $1.414v_S$. Tests show that the value of the nucleation speed does not affect the steady-state supershear speed (Fig S3). To study self-arresting and runaway ruptures, we use a sub-Rayleigh nucleation speed of $0.5v_S$.

We use the spectral element software SPECFEM3D[33–36] for the dynamic simulation. All the simulations are conducted on a medium-scale computing cluster with 64 cores and 384 GB memory. We set the time step based on the Courant-Friedrichs-Lewy stability condition. To guarantee sufficient numerical resolution, we set a grid size much smaller than the characteristic frictional length, i.e., $L_c/\Delta x = 10$. We also test a few models with refined grid, $L_c/\Delta x = 20$, and find their results are the same.

A2. Calculations of rupture speed We compute two types of rupture speed: depth-averaged real speed v_r and apparent horizontal speed v_r^{hor} (Fig S1a). The real speed is computed at each point on the fault from the gradient of rupture time $t(x_1, x_3)$

$$v_r^{real}(x_1, x_3) = \frac{1}{\sqrt{(\partial t/\partial x_1)^2 + (\partial t/\partial x_3)^2}} \tag{5}$$

where x_1 and x_3 are the along-strike and along-dip distances, respectively. The horizontal apparent speed is based on the horizontal gradient of rupture time:

$$v_r^{hor}(x_1, x_3) = \frac{1}{\partial t / \partial x_1}. \tag{6}$$

We averaged the real speed and apparent horizontal speed along depth at each along-strike position.

A3. Energy release rate for in-plane supershear rupture The 2D theory predicts the energy release rate of supershear ruptures has the following form[37]:

$$G = g(v_r) \frac{\Delta\tau^2 L}{\mu} (\frac{\Lambda}{L})^{p(v_r)} \tag{7}$$

where $g(v_r)$ and $p(v_r)$ are known functions of rupture speed, L is the rupture propagation distance, and Λ is the size of the dynamic cohesive zone, $\Lambda \propto L_c$. In general, $g(v_r)$ depends on the shape of the slip-weakening curve[37], but in this study the friction law is fixed. In 2D, G increases from 0 at $v_r = v_S$ to its peak value at $v_r = v_E$, and then decreases to 0 at $v_r = v_P$. As $p(v_r) < 1$ for all speeds between v_S and v_P, $G \propto L^{1-p(v_r)}$ is a monotonously increasing function of L. Hence, for a constant fracture energy G_c, the rupture speed v_r approaches the P wave speed as L grows. Only if the fracture energy is scale-dependent in the form $G_c \propto L^{1-p(v_r)}$ can steady supershear ruptures exist. Otherwise the only admissible steady speed is the P wave speed. For elongated ruptures in 3D, the theory by Weng and Ampuero[15] predicts that G saturates when the rupture reaches a finite width W; it becomes a function of W instead of L. Here, we make heuristic modifications to equation (7) by replacing L with W:

$$G = g(v_r)(\frac{\Lambda}{W})^{p(v_r)} G_0. \tag{8}$$

Here $g(v_r)$ differs from the one in the 2D theory by a geometrical factor of order 1. The energy balance $G = G_c$ gives

$$\frac{G_c}{G_0} = g(v_r)(\frac{\Lambda}{W})^{p(v_r)} \tag{9}$$

We suppose that, like in the 2D case, the right side of the above equation also increases from 0 at $v_r = v_S$ to its peak at $v_r = v_E$, and then decreases to 0 at $v_r = v_P$. This equation of motion of mode II long ruptures predicts that supershear propagation is stable if the energy ratio is below the maximum of the right side of equation 9, which is numerically estimated as $g(v_E) \approx 0.9$ (note that $p(v_E) = 0$). If $G_c/G_0 < 0.9$, there are two mathematical solutions of this equation of motion, one with speed between v_S and v_E and the other between v_E and v_P. Only the latter is stable, because the velocity-decreasing energy release rate provides a negative feedback to any perturbation of rupture speed, which stabilizes steady ruptures. In our 3D purely mode II dynamic simulations, we only observe steady supershear ruptures at speeds between v_E and v_P, which is well explained by the heuristic equation of motion.

A4. Energy release rate for mixed-mode rupture For mixed-mode ruptures in 3D faults with finite width W, we use a reduced-dimensionality (2.5D) model to derive the energy release rate. The 2.5D model has been proved to be a very good approximation of the 3D elongated rupture model[15]. It assumes that the rupture front is nearly vertical. In the 3D dynamic simulations, the angles of mixed-mode rupture front are quite small ($<10°$) for fast supershear, sub-shear runaway and self-arresting ruptures (Fig 2d). For slow supershear and "forbidden" speeds, the rupture front tilt is substantial and its effects can not be ignored.

The energy release rate is the rate of mechanical energy flow into the rupture tip per unit rupture advance. The stress drop vector (fault-parallel traction change) is approximately parallel to the slip vector, because we focus on situations with little rake rotation. The total energy release rate for a mixed-mode is the sum of the mode II and III contributions, which are associated to the along-strike $\Delta\tau_{str} = \Delta\tau\cos\theta$ and along-dip $\Delta\tau_{dip} = \Delta\tau\sin\theta$ components of stress drop, respectively:

$$G^{mix} = G^{II}\cos^2\theta + G^{III}\sin^2\theta \tag{10}$$

where G^{II} and G^{III} denote the energy release rates of purely mode II and III ruptures, respectively, that would prevail if both modes had the same stress drop $\Delta\tau$.

Equation (10) can be understood by a circular shear crack model[38]. The stress intensity factors at any point along a static circular rupture front of radius a are

$$K_{II} \propto \Delta\tau\sqrt{a}\cos\omega; \quad K_{III} \propto \Delta\tau\sqrt{a}\sin\omega \tag{11}$$

where ω is the angle between the slip direction and the local rupture propagation direction. The expressions have a similar form at the major axis tip of an elliptical rupture, which can be set horizontal for analogy to the 2.5D model, provided a is the small axis length. Considering the energy release rate from each mode is proportional to the square of its stress intensity factor[39], the total energy release rate at the rupture front propagating in the horizontal direction has a similar form to equation (10).

Based on 2.5D models (Methods A1 and A3):

$$G^{II} = \begin{cases} (1-\nu)^{-1} G_0, & \text{if } v_r < v_R \\ G^{II}_{fb}, & \text{if } v_R < v_r < v_S \\ g(v_r)(\frac{\Lambda}{W})^{p(v_r)} G_0, & \text{if } v_S < v_r < v_P \end{cases} \tag{12}$$

and

$$G^{III} = \begin{cases} G_0, & \text{if } v_r < v_S \\ G^{III}_{Sup}. & \text{if } v_r > v_S \end{cases} \tag{13}$$

where $G_0 = \lambda_{III} \Delta\tau^2 W/\mu$ and v_r is the depth-averaged real speed. The 2D analytical solutions of G^{II}_{fb} and G^{III}_{Sup} depend on the mathematical assumption[12,16,40]. One solution suggests that G^{II}_{fb} and G^{III}_{Sup} have the same forms as for sub-Rayleigh ruptures but with negative values, which are $G^{II}_{fb} = -(1-\nu)^{-1} G_0$ and $G^{III}_{Sup} = -G_0$ for 2.5D models. Another solution suggests they equal zero. The results of 2D numerical simulations[16] lie between the two theoretical solutions. Therefore, we suggest these two theoretical solutions are two end-members and suppose G^{II}_{fb}/G_0 has a value between $-(1-\nu)^{-1}$ and 0 and G^{III}_{Sup}/G_0 has a value between -1 and 0.

Self-arresting ruptures occur if the energy release rate of mixed-mode steady ruptures is too small to match the fracture energy, $G_c > G^{mix}$. Runaway ruptures near the boundary with self-arresting ruptures have sub-Rayleigh speeds and almost vertical fronts ($< 5°$). Thus the theoretical boundary between self-arresting and runaway ruptures corresponds to the condition $G_c = G^{mix}$ evaluated at sub-Rayleigh speeds ($v_r < v_R$):

$$G_c/G_0 = (1-\nu)^{-1} \cos^2\theta + \sin^2\theta. \tag{14}$$

The theoretical boundary between fast supershear and slow supershear ruptures is obtained by evaluating the energy balance $G_c = G^{mix}$ at $v_r = v_E$:

$$G_c = g(v_E) G_0 \cos^2\theta + G^{III}_{Sup} \sin^2\theta \tag{15}$$

where $(\frac{\Lambda}{W})^{p(v_E)} = 1$ because $p(v_E) = 0$ and we know that $g(v_E) = 0.9$ (Methods A3). We find that if we set $G^{III}_{Sup}/G_0 = -0.4$ (amid the two end-member analytical solutions) the resulting equation fits well the Eshelby boundary from our 3D dynamic simulations:

$$G_c/G_0 = 0.9\cos^2\theta - 0.4\sin^2\theta. \tag{16}$$

For the boundary between supershear and subshear regimes, the theoretical relation is

$$G_c = g(v_{S+})(\frac{\Lambda}{W})^{p(v_{S+})} G_0 \cos^2\theta + G^{III}_{Sup} \sin^2\theta \tag{17}$$

where v_{S+} is a rupture speed slightly larger than the S wave speed. Near this boundary, the rupture front tilts severely, $\sim$30° (Fig 2d), thus the effects of tilted rupture front needs to be considered. The first term on the right side of equation (17) is positive and the second term is non positive. The first term on the right side of equation (17) need to be sufficient to support the dissipated fracture energy. As the term $g(v_{S+})$ is quite small according to the theory (Methods A3), we suppose that the geometrical effect of tilted front enlarges the size of the "apparent cohesive zone" along the strike direction to make the first term sufficiently large. We find that if we set $g(v_{S+})(\frac{\Lambda}{W})^{p(v_{S+})} = 0.9$ (same as equation (16)) and $G^{III}_{Sup}/G_0 = 0.0$ (one end-member analytical solution) the resulting equation fits well the supershear boundary for small rake angle

$$G_c/G_0 = 0.9\cos^2\theta. \tag{18}$$

For larger rake angle, equation (18) underestimates the energy release rate due to the even larger tilt of the rupture front (>30°, Fig 2d).

A5. Scaling relation of energy release rate On long faults, the static energy release rate $G_0(x)$ is related to final slip $D(x)$ by

$$G_0(x) = \frac{1}{2}\int_0^W \Delta\tau(x,z)D(x,z)dz \tag{19}$$

where x and z are along-strike and along-dip distances, respectively. To first order, $\Delta\tau(x) = 2C\mu D(x)/W$, thus this equation is approximated as

$$G_0(x) = \frac{C\mu D(x)^2}{W} = \frac{1}{4C}\frac{\Delta\tau(x)^2 W}{\mu} \tag{20}$$

where C is a geometrical factor of order 1 and $\Delta\tau(x)$ and $D(x)$ are the depth-averaged stress drop and slip, respectively. For a very long mode III rupture with constant stress drop, the static factor[41] relating stress drop $\Delta\tau$ and final average slip D on a deep buried fault is $C = \pi/4$. Comparing equation (20) with the definition of mode II energy release rate (Methods A1), we have $C = 1/(\lambda_{III})$, which is consistent with the static factor[41] on a deep buried fault. For mode II rupture, $\lambda_{II}/\lambda_{III} = (1-\nu)^{-1}$ and thus $C = (1-\nu)\pi/4$, where ν is the Poisson's ratio. For a mixed-mode rupture,

$$\begin{aligned}
\Delta\tau^2 &= \Delta\tau_{str}^2 + \Delta\tau_{dip}^2 \\
\Delta\tau_{str} &= \frac{(1-\nu)\pi\mu}{4W}D_{str} \\
\Delta\tau_{dip} &= \frac{\pi\mu}{4W}D_{dip}.
\end{aligned} \tag{21}$$

Since we focus on situations with little rake rotation, we have

$$D_{str} = D \cos\theta$$
$$D_{dip} = D \sin\theta. \tag{22}$$

Therefore, the factor relating stress drop $\Delta\tau$ and final average slip D for mixed-mode rupture is

$$C = \frac{\pi}{4}\sqrt{(1-\nu)^2\cos^2\theta + \sin^2\theta} \tag{23}$$

A6. Kinematic model To investigate the possible reasons of unexpected steady speeds, we compare the dynamic models with a simple kinematic model designed to capture purely-geometric effects (Fig S4a). We assume that a supershear rupture extends as an elliptical front propagating at the P wave speed along its major axis and at the S wave speed along its minor axis, the limiting speeds for mode II and III ruptures, respectively. The elliptical fronts are truncated to lie inside the seismogenic portion of the fault. The rake angle is the angle between the major axis of the ellipse and the strike direction. We vary the rake angle and compute the depth-averaged real speed, the horizontal speed and the depth-averaged rupture propagation angle (angle of the real rupture speed relative to the horizontal direction).

We find that the basic geometrical effects of tilted elliptical front represented in the kinematic model only account for part of the dynamic simulation results. The rupture speeds decrease as the rake angle increases (Fig S4b and S4c), as in the dynamic models, but there are also important discrepancies between the two models. Beyond a rake of 20-30°, the speed of the dynamic models decreases faster than that of the kinematic models. An eventual drop to sub-Rayleigh speeds is only found in the dynamic models. Furthermore, the variability of the real speed across the depth profile is larger in the dynamic model than in the kinematic model. The dependency of the rupture propagation angle as a function of rake angle (Fig S4d) is totally different between the two models. Also, the variability across depth of the rupture angle is much larger in the dynamic model than in the kinematic model, which means the curvature of the dynamic front is larger than that of the kinematic elliptical front. The rupture angle drops to less than 10° once the speed drops below the Rayleigh speed, only in the dynamic models.

1. Gabriel, A., Ampuero, J., Dalguer, L. & Mai, P. M. Source properties of dynamic rupture pulses with off-fault plasticity. *Journal of Geophysical Research* **118**, 4117–4126 (2013).

2. Dunham, E. M. & Bhat, H. S. Attenuation of radiated ground motion and stresses from three-dimensional supershear ruptures. *Journal of Geophysical Research: Solid Earth* **113** (2008).

3. Andrews, D. Ground motion hazard from supershear rupture. *Tectonophysics* **493**, 216–221 (2010).

4. Chounet, A., Vallée, M., Causse, M. & Courboulex, F. Global catalog of earthquake rupture velocities shows anticorrelation between stress drop and rupture velocity. *Tectonophysics* **733**, 148–158 (2018).

5. Bao, H. *et al.* Early and persistent supershear rupture of the 2018 magnitude 7.5 palu earthquake. *Nature Geoscience* (2019). URL `https://doi.org/10.1038/s41561-018-0297-z`.

6. Zhan, Z., Helmberger, D. V., Kanamori, H. & Shearer, P. M. Supershear rupture in a mw 6.7 aftershock of the 2013 sea of okhotsk earthquake. *Science* **345**, 204–207 (2014).

7. Bouchon, M. *et al.* How fast is rupture during an earthquake? new insights from the 1999 turkey earthquakes. *Geophysical Research Letters* **28**, 2723–2726 (2001).

8. Bouchon, M. & Vallée, M. Observation of long supershear rupture during the magnitude 8.1 kunlunshan earthquake. *Science* **301**, 824–826 (2003).

9. Yue, H. *et al.* Supershear rupture of the 5 january 2013 craig, alaska (mw 7.5) earthquake. *Journal of Geophysical Research* **118**, 5903–5919 (2013).

10. Wang, D. & Mori, J. Short-period energy of the 25 april 2015 mw 7.8 nepal earthquake determined from backprojection using four arrays in europe, china, japan, and australia. *Bulletin of the Seismological Society of America* **106**, 259–266 (2016).

11. Hicks, S. *et al.* Back-propagating super-shear rupture in the 2016 m7. 1 romanche transform fault earthquake. *Eartharxiv* (2019).

12. Burridge, R. Admissible speeds for plane-strain self-similar shear cracks with friction but lacking cohesion. *Geophysical Journal International* **35**, 439–455 (1973).

13. Mai, P. M. & Thingbaijam, K. Srcmod: An online database of finite-fault rupture models. *Seismological Research Letters* **85**, 1348–1357 (2014).

14. Song, X. *et al.* Geodetic observations of the 2018 mw 7.5 sulawesi earthquake and its implications for the kinematics of the palu fault. *Geophysical Research Letters* **46**, 4212–4220 (2019).

15. Weng, H. & Ampuero, J. The dynamics of elongated earthquake ruptures. *Journal of Geophysical Research: Solid Earth* (2019).

16. Andrews, D. Dynamic growth of mixed-mode shear cracks. *Bulletin of the Seismological Society of America* **84**, 1184–1198 (1994).

17. Bizzarri, A. & Das, S. Mechanics of 3-d shear cracks between rayleigh and shear wave rupture speeds. *Earth and Planetary Science Letters* **357**, 397–404 (2012).

18. Ampuero, J. & Mao, X. Upper limit on damage zone thickness controlled by seismogenic depth. *Fault Zone Dynamic Processes: Evolution of Fault Properties During Seismic Rupture* **227**, 243 (2017).

19. Fang, J. *et al.* The 2018 mw 7.5 palu earthquake: A supershear rupture event constrained by insar and broadband regional seismograms. *Remote Sensing* **11**, 1330 (2019).

20. Oral, E., Weng, H. & Ampuero, J. P. Does a damaged-fault zone mitigate the near-field impact of supershear earthquakes?—application to the 2018 mw 7.5 palu, indonesia earthquake. *Geophysical Research Letters* e2019GL085649 (2020).

21. Mai, P. *et al.* On scaling of fracture energy and stress drop in dynamic rupture models: Consequences for near-source ground-motions. *Earthquakes: Radiated Energy and the Physics of Faulting* 283–293 (2006).

22. Weng, H. & Yang, H. Constraining frictional properties on fault by dynamic rupture simulations and near-field observations. *Journal of Geophysical Research* (2018).

23. Gallovič, F., Valentová, L., Ampuero, J. & Gabriel, A. Bayesian dynamic finite-fault inversion: 1. method and synthetic test. *Journal of Geophysical Research: Solid Earth* (2019).

24. Nielsen, S. *et al.* G: Fracture energy, friction and dissipation in earthquakes. *Journal of Seismology* 1–19 (2016).

25. Viesca, R. C. & Garagash, D. I. Ubiquitous weakening of faults due to thermal pressurization. *Nature Geoscience* **8**, 875–879 (2015).

26. Tinti, E., Cocco, M., Fukuyama, E. & Piatanesi, A. Dependence of slip weakening distance (dc) on final slip during dynamic rupture of earthquakes. *Geophysical Journal International* **177**, 1205–1220 (2009).

27. Andrews, D. Rupture dynamics with energy loss outside the slip zone. *Journal of Geophysical Research* **110** (2005).

28. Moreno, M. *et al.* Heterogeneous plate locking in the south–central chile subduction zone: Building up the next great earthquake. *Earth and Planetary Science Letters* **305**, 413–424 (2011).

29. Jolivet, R., Simons, M., Agram, P., Duputel, Z. & Shen, Z. Aseismic slip and seismogenic coupling along the central san andreas fault. *Geophysical Research Letters* **42**, 297–306 (2015).

30. Villegas-Lanza, J. C. *et al.* Active tectonics of peru: Heterogeneous interseismic coupling along the nazca megathrust, rigid motion of the peruvian sliver, and subandean shortening accommodation. *Journal of Geophysical Research: Solid Earth* **121**, 7371–7394 (2016).

31. Weng, H. & Yang, H. Seismogenic width controls aspect ratios of earthquake ruptures. *Geophysical Research Letters* **44**, 2725–2732 (2017).

32. Day, S., Dalguer, L., Lapusta, N. & Liu, Y. Comparison of finite difference and boundary integral solutions to three-dimensional spontaneous rupture. *Journal of Geophysical Research* **110**, B12307 (2005).

33. Ampuero, J. Etude physique et numérique de la nucléation des séismes. *PhD Thesis, University of Paris VII, France* (2002).

34. Komatitsch, D. & Vilotte, J.-P. The spectral element method: an efficient tool to simulate the seismic response of 2d and 3d geological structures. *Bulletin of the seismological society of America* **88**, 368–392 (1998).

35. Galvez, P., Ampuero, J.-P., Dalguer, L. A., Somala, S. N. & Nissen-Meyer, T. Dynamic earthquake rupture modelled with an unstructured 3-d spectral element method applied to the 2011 m 9 tohoku earthquake. *Geophysical Journal International* **198**, 1222–1240 (2014).

36. Kaneko, Y., Lapusta, N. & Ampuero, J. Spectral element modeling of spontaneous earthquake rupture on rate and state faults: Effect of velocity-strengthening friction at shallow depths. *Journal of Geophysical Research* **113**, B09317 (2008).

37. Broberg, K. Intersonic bilateral slip. *Geophysical Journal International* **119**, 706–714 (1994).

38. Tada, H., Paris, P. C., Irwin, G. R. & Tada, H. *The stress analysis of cracks handbook*, vol. 130 (ASME press New York, 2000).

39. Freund, L. *Dynamic fracture mechanics* (Cambridge university press, 1998).

40. Freund, L. & Clifton, R. On the uniqueness of plane elastodynamic solutions for running cracks. *Journal of elasticity* **4**, 293–299 (1974).

41. Luo, Y., Ampuero, J.-P., Miyakoshi, K. & Irikura, K. *Surface rupture effects on earthquake moment-area scaling relations*, 7–18 (Springer, 2018).

Acknowledgements The open-source software SPECFEM3D used in our 3-D dynamic rupture simulations is available from the Computational Infrastructure for Geodynamics at https://geodynamics.org/cig/software/specfem3d/. This work was supported by the French government through the Investments in the Future project UCAJEDI (ANR-15-IDEX-01) managed by the French National Research Agency (ANR). We thank Diego Molina for providing the central Andes coupling model in digital form.

Correspondence Correspondence and requests for materials should be addressed to Huihui Weng (email: weng@geoazur.unice.fr).

Figure 1 Long rupture propagating on a fault with finite width W and oblique slip (rake angle defined between slip and strike directions). The inset shows the propagation of a tilted rupture front on a fault, arrows show the local direction of rupture speed.

Figure 2 (a) Five different rupture behaviours (see legend) as a function of energy ratio G_c/G_0 and rake angle θ from a systematic set of 3D dynamic rupture simulations. Black curves are the theoretical estimates explained in Methods A4. (b) Normalized depth-averaged rupture speed v_r/v_S (colored curves coded by rake angle) as a function of normalized distance L/W from models with $G_c/G_0 = 0.63$. v_R, v_S, v_E, and v_P are the Rayleigh wave, shear wave, Eshelby, and P wave speeds, respectively. (c) Dependencies of normalized steady supershear speed (depth-averaged) on energy ratio and rake angle. (d) Dependencies of real speed angle (depth-averaged) on energy ratio and rake angle. Note that the real speed angle has opposite rotation relative to the rake angle. Gray region indicates subshear ruptures whose real speed angle is smaller than 5°.

Figure 3 (a) Observed rupture speed and rake angle of global earthquakes (colored symbols coded by aspect ratio). The rupture speeds are compiled from various references[4–11]. The rake angles and the aspect ratios are compiled from USGS and SRCMOD[13]. The shear wave speeds used to normalize the rupture speed are either from their original papers or from 1D PREM model. The events with unknown aspect ratios are presented as white symbols. Black solid curves indicate the contours of energy ratio ($>$0.5) in 3D numerical simulations. Black dash curves and arrow indicate qualitatively the position of contours for smaller energy ratios (<0.5) deduced from theory (Methods A1). (b) Bottom: cartoon showing five different rupture behaviours in (G_c/G_0, θ) space derived from the 3D numerical simulations and theory. Numbers indicate the critical energy ratios at several points. Top: continuum of steady and average rupture speed as a function of energy ratio for a fixed rake angle as shown in the profile AA' in the bottom plot. Purple curves indicate the steady-state rupture speeds. Black curve indicates the average rupture speeds as a function of energy ratio, with fixed rupture length and initial rupture speed. Gray box shows all possible average rupture speeds for various rupture length and initial rupture speed.

Figure 4 (a) Estimated fracture energy G_c versus final slip D over a wide range of event sizes derived from various references[21–25], laboratory experiments[24]. The black thick line is the power-law fitting curve for the results of dynamic models and lab experiments with $D > 0.1m$. The thin black lines are the theoretical relations between energy release rate G_0 and final slip D on long faults for different seismic widths. (b) Distribution of slip deficit rate of the southern Andes subduction zone, Chile (left) and depth-averaged slip deficit rate along strike (right). The slip deficit rate is the product of a seismic coupling model inferred from geodetic data[28] and a constant plate convergence rate ~66 mm/yr. The epicenter (red star) and rough rupture region (green curve) of the 1960 Valdivia earthquake are shown. The rake angle between the Nazca Plate convergence and strike direction is $\sim 60°$. (c) Elapsed time for the fault to accumulate the critical slip deficit for runaway rupture, $D = D^{run}$, after the 1960 earthquake that is assumed to have released all the slip deficit. The colored band accounts for uncertainties in the $G_c - D$ scaling relation. The fault is partitioned into segments with runaway and self-arresting behavior, and this segmentation evolves with time (runaway segments are shown by blue lines at three times).

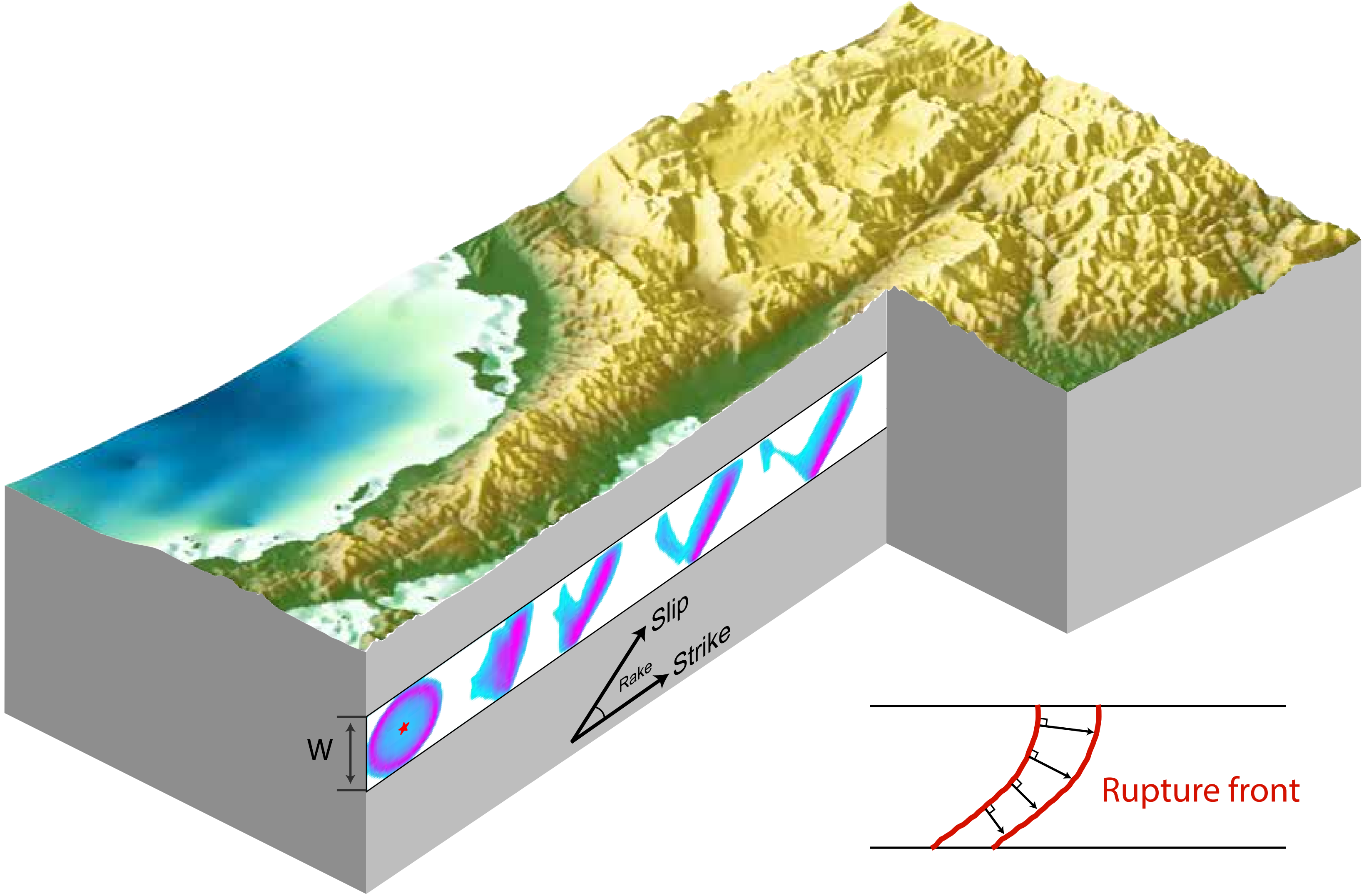
Slip
Strike
Rake
W
Rupture front

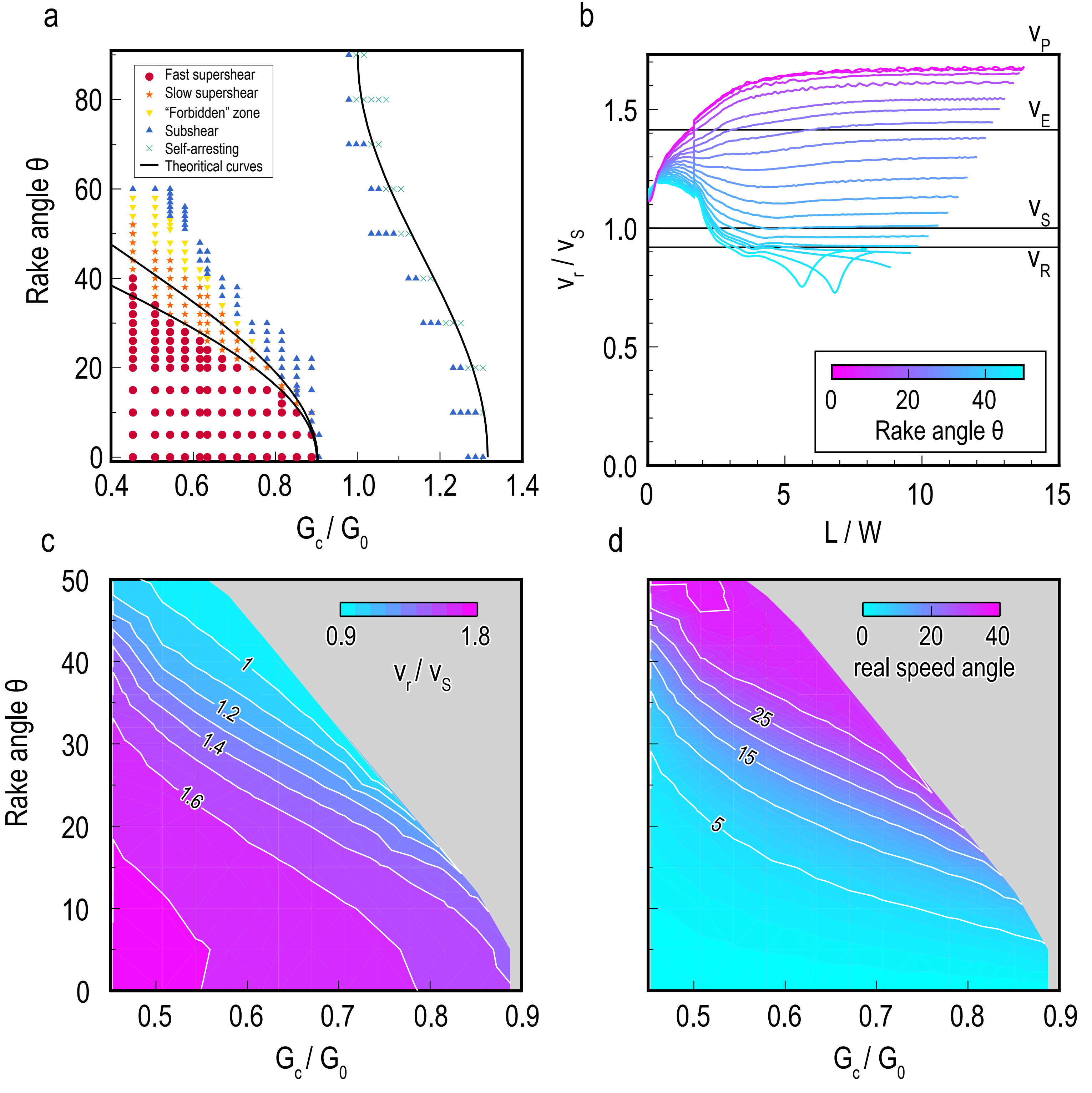

a
Fast supershear
Slow supershear
“Forbidden” zone
Subshear
Self-arresting
Theoritical curves
Rake angle θ
G_c / G_0
b
v_P
v_E
v_S
v_R
v_r / v_S
L / W
Rake angle θ
c
v_r / v_S
Rake angle θ
G_c / G_0
d
real speed angle
G_c / G_0

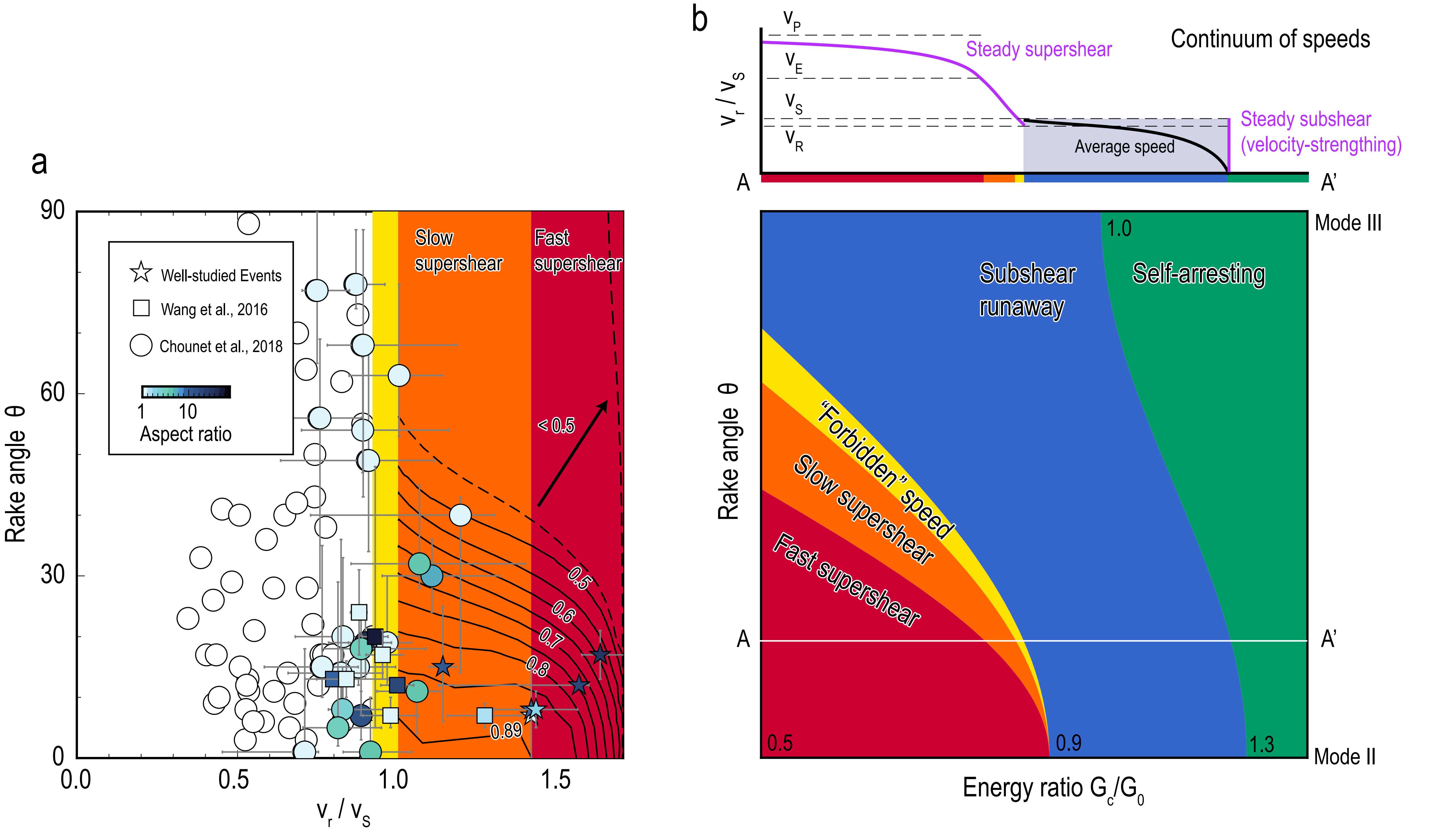

a
b
Well-studied Events
Wang et al., 2016
Chounet et al., 2018
1
10
Aspect ratio
Slow supershear
Fast supershear
< 0.5
0.5
0.6
0.7
0.8
0.89
Rake angle θ
v_r / v_S
0.0
0.5
1.0
1.5
0
30
60
90
v_P
v_E
v_S
v_R
v_r / v_S
Steady supershear
Continuum of speeds
Steady subshear
(velocity-strengthing)
Average speed
A
A'
Mode III
Mode II
Subshear runaway
Self-arresting
"Forbidden" speed
Slow supershear
Fast supershear
1.0
0.5
0.9
1.3
Rake angle θ
Energy ratio G_c/G_0

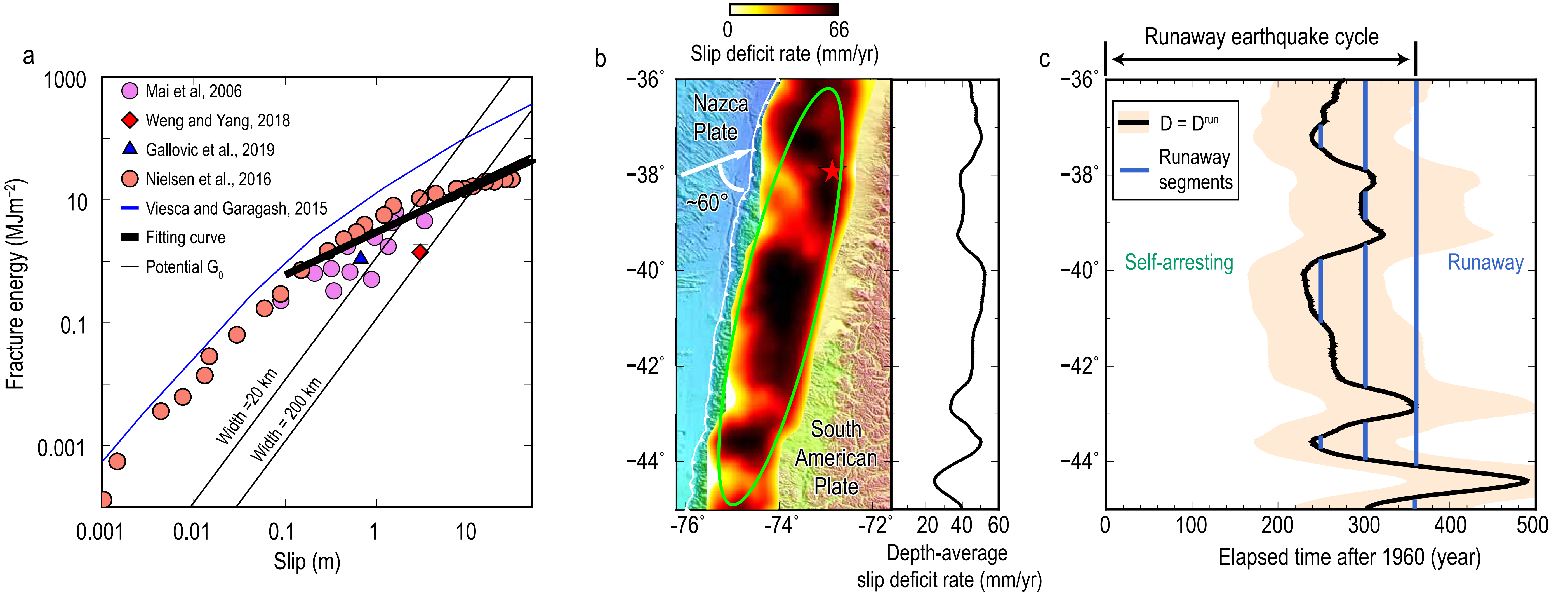

a
Mai et al, 2006
Weng and Yang, 2018
Gallovic et al., 2019
Nielsen et al., 2016
Viesca and Garagash, 2015
Fitting curve
Potential G_0
Fracture energy (MJm^{-2})
1000
10
0.1
0.001
Width =20 km
Width = 200 km
0.001
0.01
0.1
1
10
Slip (m)
b
0
66
Slip deficit rate (mm/yr)
Nazca Plate
~60°
South American Plate
−36˚
−38˚
−40˚
−42˚
−44˚
-76˚
-74˚
-72˚
20
40
60
Depth-average slip deficit rate (mm/yr)
c
Runaway earthquake cycle
$D = D^{run}$
Runaway segments
Self-arresting
Runaway
−36˚
−38˚
−40˚
−42˚
−44˚
0
100
200
300
400
500
Elapsed time after 1960 (year)

Oblique slip on long faults enables a continuum of earthquake rupture speeds

Huihui Weng[1] and Jean-Paul Ampuero[1]

[1]*Université Côte d'Azur, IRD, CNRS, Observatoire de la Côte d'Azur, Géoazur, 250 rue Albert Einstein, Sophia Antipolis, 06560 Valbonne, France*

Contents

4 Supplementary Figures

Figure S1.

Figure S2.

Figure S3.

Figure S4.

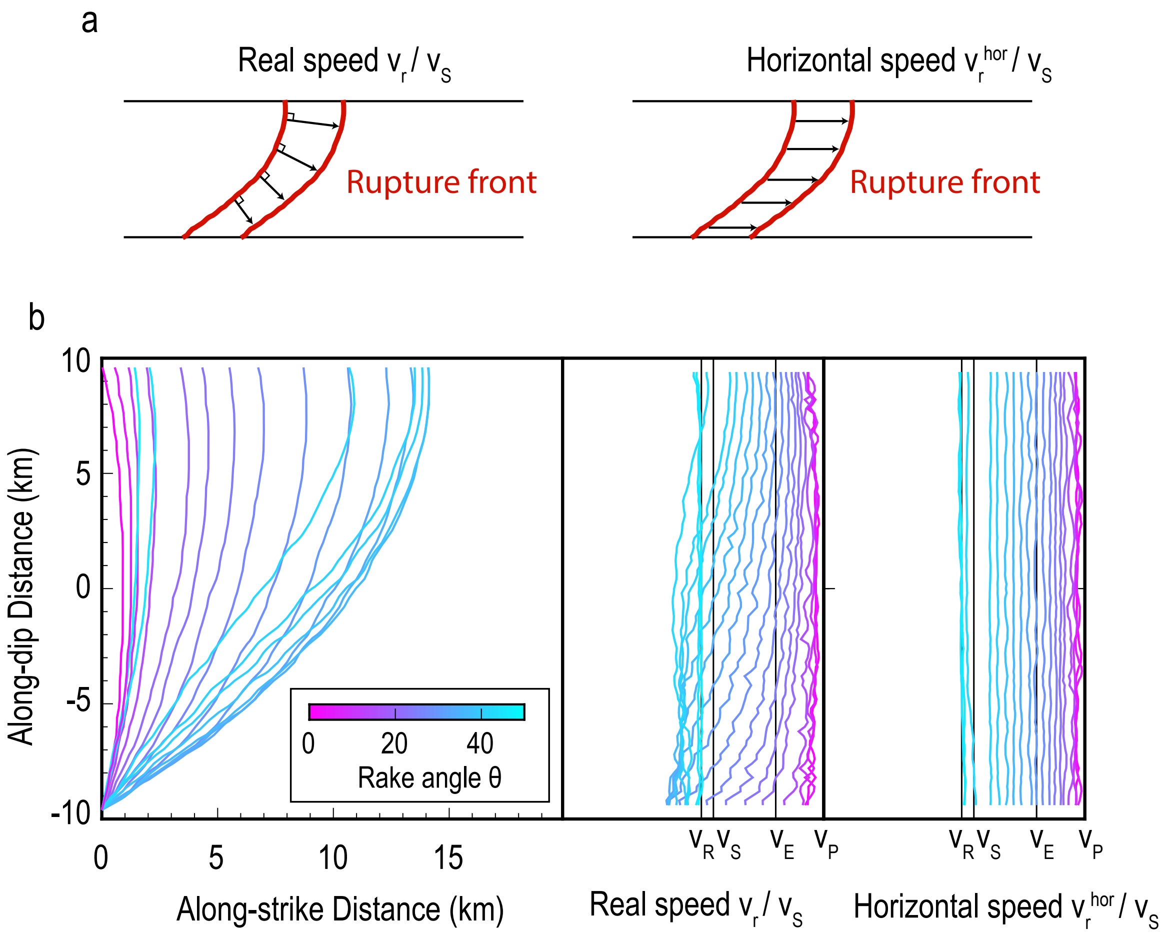

Figure S1: (a) The definition of real speed and apparent horizontal speed. (b) The shape (left), distributions of real speed (middle) and horizontal speed (right) of steady rupture fronts across the depth (colored symbols coded by rake angle).

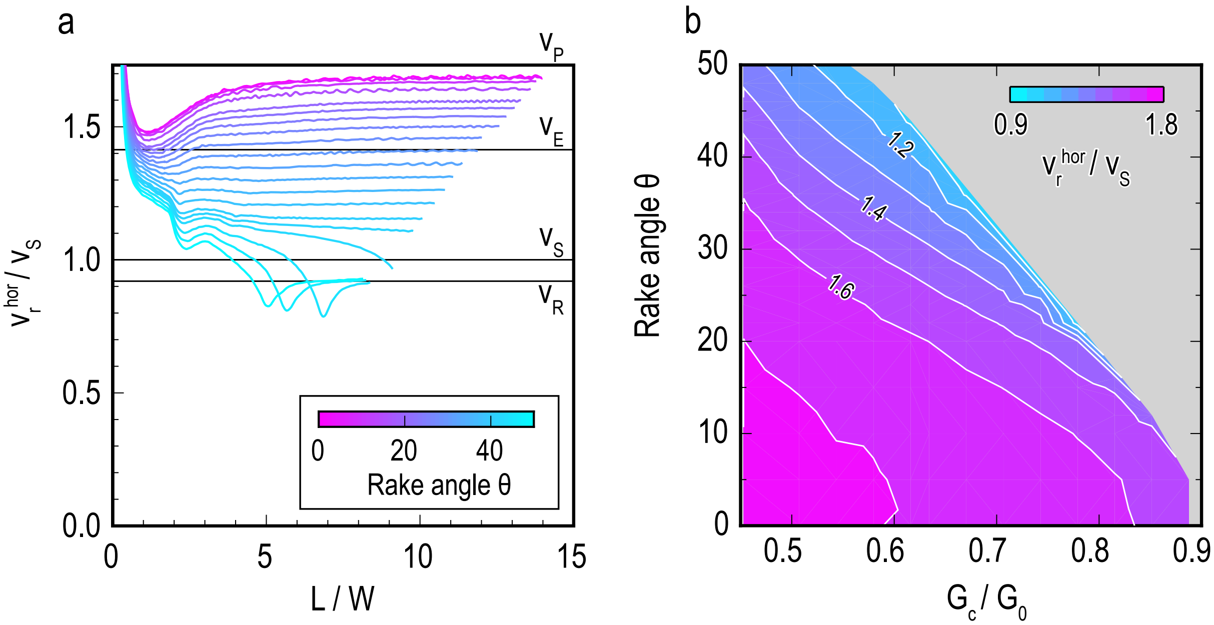

Figure S2: (a) Normalized depth-averaged horizontal speed v_r^{hor} (colored curves coded by rake angle) as a function of normalized distance L/W from the 3D dynamic rupture simulations with $G_c/G_0 = 0.63$. (b) Dependencies of normalized depth-averaged horizontal speed on energy ratio and rake angle.

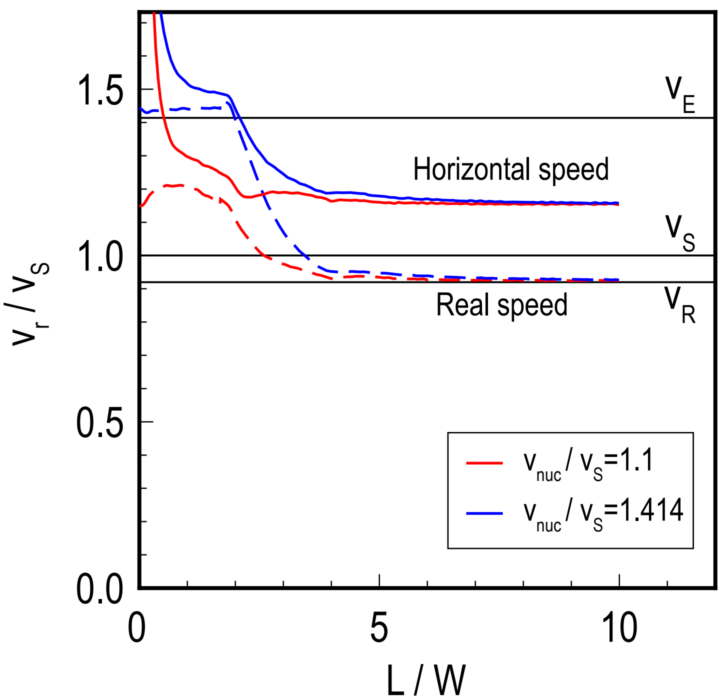

Figure S3: Normalized depth-averaged speeds as a function of normalized distance L/W from the 3D dynamic rupture simulations with different nucleation speeds.

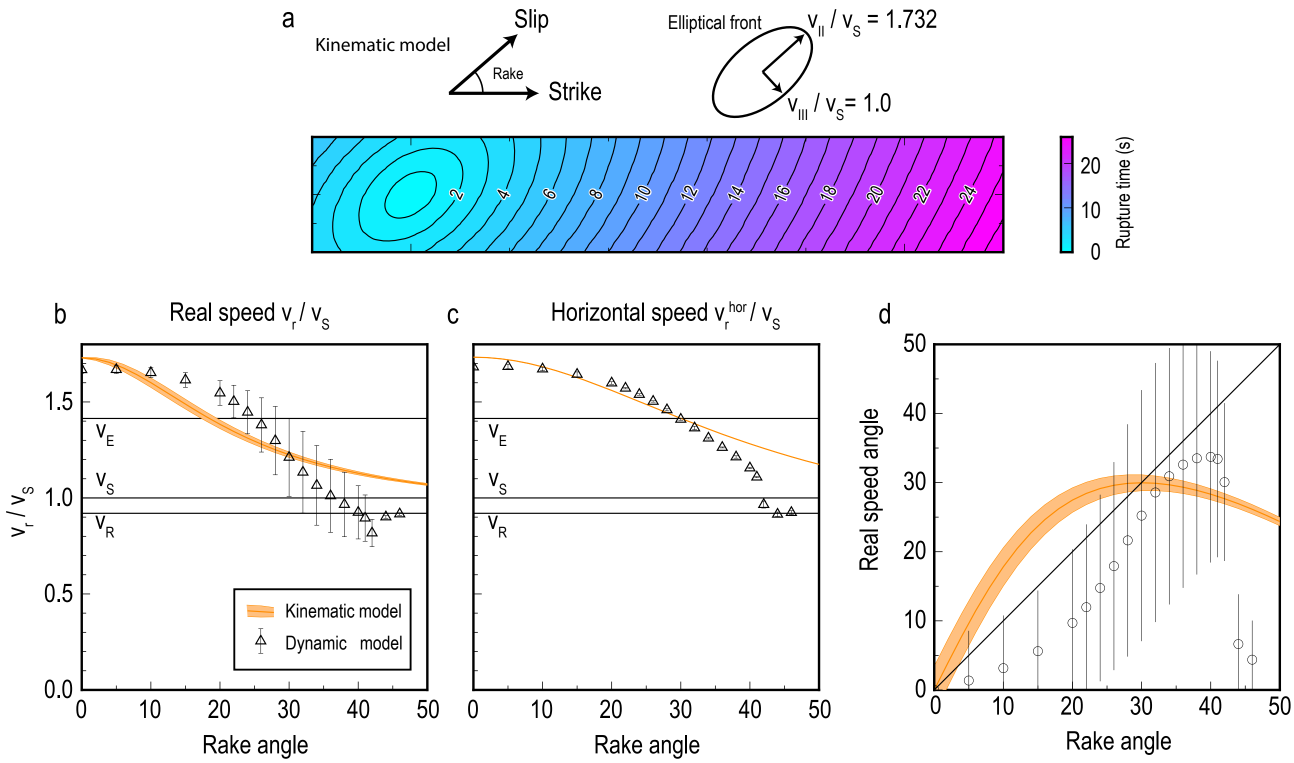

Figure S4: (a) Rupture contours of a kinematic model with oblique slip whose rupture extends as an elliptical front propagating at the P wave speed along its major axis and at the S wave speed along its minor axis. The rake angle is the angle between the major axis of the ellipse and the strike direction. (b) The comparison of depth-averaged real speed between the kinematic and dynamic models with $G_c/G_0 = 0.63$ versus rake angle. The definition of real speed and horizontal speed are the same for both the kinematic and dynamic models. (c) The comparison of horizontal speed versus rake angle. (d) Dependency of depth-averaged real speed angle on rake angle for both kinematic and dynamic models.